Cyclic Permeability Evolution During Repose Then Reactivation of Fractures and Faults

Kyungjae Im[1,2] (ID), **Derek Elsworth[1]** (ID), and **Chaoyi Wang[1,3]** (ID)

[1]Department of Energy and Mineral Engineering, EMS Energy Institute, and G3 Center, The Pennsylvania State University, University Park, PA, USA, [2]Now at Geology and Planetary Science Division, California Institute of Technology, Pasadena, CA, USA, [3]Now at Department of Physics and Astronomy, Purdue University, West Lafayette, IN, USA

Abstract Cyclic growth and decay of permeability in fractures is explored during repeated reactivation and repose of saw-cut fractures of Green River shale. These slide-hold-slide experiments are supported by measurements of fracture normal deformation and optical surface profilometry. Overall, we observe continuous permeability decay during repose (holds) and significant permeability enhancement during slow reactivation (slide). The permeability decay is accompanied by fault compaction. Both hydraulic aperture change (Δb_h) and measured compaction (Δb_s) are consistent with time-dependent power law closure with a power exponent of ~0.2–0.4. These dual compaction magnitudes are positively correlated but $\Delta b_h > \Delta b_s$ in late stage holds. Permeability enhancement during reactivation is typically also accompanied by fault dilation. However, we also observe some cases where hydraulic aperture change decouples from the measured deformation, conceivably driven by mobilization of wear products and influenced by the development of flow bottlenecks. Pretest and posttest surface profiles show that the surface topography of the fractures is planed down by shear removal. The shear removal is significant with initial laboratory prepared surface (~10 μm of aperture height) but less significant following consecutive reactivations (~2 μm). The flattened surfaces retain small-scale, ~10–20 μm wavelength, roughness. Flow simulations, constrained by the surface topography and measured deformation, indicate that small-scale roughness may control permeability at flow bottlenecks within a dominant flow channel. These results suggest cycles of permeability creation and destruction are an intrinsic component of the natural hydraulic system present in faults and fractures and provide an improved mechanistic understanding of the evolution of permeability during fault repose and reactivation.

1. Introduction

Permeability evolution of fractures and faults is crucial in understanding the response of the natural hydraulic system to static and dynamic stress perturbations during the earthquake cycle (Brodsky et al., 2003; Elkhoury et al., 2006; Manga et al., 2003, 2012; Wang & Manga, 2015; Wang et al., 2016; Xue et al., 2013), and in the engineering of petroleum, geothermal, and CO_2 sequestration reservoirs (Fang et al., 2017; Mukuhira et al., 2017; Zoback et al., 2012). One of the major concerns of fracture permeability is in response to shear reactivation as it is widely observed that the permeability of natural faults is significantly enhanced with shear reactivation (Elkhoury et al., 2006; Guglielmi et al., 2015; Mukuhira et al., 2017; Xue et al., 2013; Zoback et al., 2012).

Fault permeability response is significantly dependent on contact matedness. Fault slip experiments and models with initially mated rough surfaces (artificially fractured or fabricated bare contact or densely packed gouge filled contact) show significant permeability enhancement with slip (e.g., Davidesko et al., 2014; Elsworth & Goodman, 1986; Fang et al., 2018; Wang et al., 2017). Conversely, when the fault is initially unmated, strong permeability reduction may result from the comminution of surface asperities (e.g., Broadky et al., 2011; Fang et al., 2017; Faoro et al., 2009; Zhang et al., 1999). These observations, together with shear permeability enhancements observed in nature, suggest that there may be a significant mating process that develops during the repose period of natural faults that primes the faults for shear permeability enhancement. Indeed, highly mated and surface correlated natural faults are reported from facing surface profiling of the contacting hanging and foot walls (Junger & Tullis, 2003; Power & Tullis, 1992). This reasoning is consistent with the studies of field scale fault reactivation that show gradual dilation at the onset of fault slip (Guglielmi et al., 2015).

Static compaction may increase asperity matedness. Slow permeability reduction under static loading has been widely observed in both laboratory experiments (Giger et al., 2007; Polak et al., 2003; Yasuhara et al., 2006) and natural hydrological systems (Elkhoury et al., 2006; Xue et al., 2013). Mechanisms of chemo-mechanical compaction, such as pressure solution, stress corrosion, and mineral precipitation (Lehner, 1995; Niemeijer et al., 2008; Yasuhara et al., 2003, 2004; Yasuhara & Elsworth, 2008) are all plausible mechanisms of inducing preslip asperity compaction of natural faults. Dissolution of asperities occurs over the microscopic contact, which is not necessarily aligned with the mesoscale fracture orientation; thus, solution-driven compaction may enhance matedness of the contact.

Roughness is an important requirement for this compaction-induced mating process. If the two contacting surfaces are perfectly flat (or mirrored), compaction does not promote contact mating since mesoscale fracture orientation and microscopic contacts are parallel. However, natural fault surfaces are never perfectly flat—rather, they exhibit scale-dependent roughness (Candela et al., 2011; Power et al., 1987; Renard & Candela, 2017; Tesei et al., 2017). Moreover, recent observations indicate that there is a small-scale (typically a few tens of microns wavelengths) minimum roughness that exists on the sheared surfaces regardless of slip direction (Candela & Brodsky, 2016).

It is shown that the permeability response in fault gouge can be significantly influenced by the preslip hold period (Chen et al., 2015; Olsen et al., 1998) and, more recently, with bare rock contacts (Im et al., 2018). The following reports permeability evolution during reactivation (slide) and repose (hold) experiments using initially unmated fault surface with concurrent measurement of fault normal deformations and separate measurement of the evolution of fracture topography both before and after the experiments.

2. Method

2.1. Slide-Hold-Slide Experiment With Permeability Measurement

We conduct fluid-flow-through double-direct-shear experiments on fractures of Green River shale constrained by additional measurements of fracture normal displacement. A saw-cut prismatic rock block ($40.0 \times 25.2 \times 3.93$ mm) is sandwiched between two half-cylindrical rock cores representing a dual fracture system—that is, the two contact surfaces between the split cores and center block (Figure 1). The experiment is controlled by three servo pumps. Pump A applies confining pressure that is maintained at 3 MPa in this experiment. The samples are hydraulically isolated by a latex jacket with normal stress applied to the exterior by pump A. The loading piston, which controls center block shear displacement, is pushed by constant flow rate of water injection from pump B. Shear displacement is measured via a linear variable differential transducer connected to the loading piston. Pump C supplies water that flows through the dual fracture surface (on both sides of the center block). Permeability is calculated by the pressure and flow rate of pump C.

Permeability (k) is calculated based on Darcy's law assuming steady state as

$$k = \frac{\mu l}{A} \frac{(Q + whV)}{\Delta P} \tag{1}$$

where μ is the fluid viscosity (8.9×10^{-4} Pa·s), l is the flow path length (25 mm), A is the cross-sectional area of the sample (core and center block) perpendicular to the flow path (4.71×10^{-4} m^2), Q is the flow rate of Pump C, w is the center block width (25.2 mm), h is the center block thickness (3.93 mm), V is the slip velocity, and ΔP is the pressure difference across the sample. The term whV in parentheses is a flow rate correction for intrusion of the sample center block.

Evolution of fracture aperture, correlating with asperity height, can be estimated by converting the flow rate to an equivalent hydraulic aperture b_h of each fracture via the cubic law relation (Witherspoon et al., 1980)

$$\frac{Q + whV}{2} = \frac{b_h{}^3 w}{12\mu} \frac{\Delta P}{l} \tag{2}$$

where the notations are identical to equation (1). Note that equivalent flow rate ($Q + whV$) is halved since our experiment embeds two fractures. Accordingly, hydraulic aperture can be defined as

$$b_h = \left(\frac{(Q + whV)}{2} \frac{l}{\Delta P} \frac{12\mu}{w} \right)^{\frac{1}{3}}. \tag{3}$$
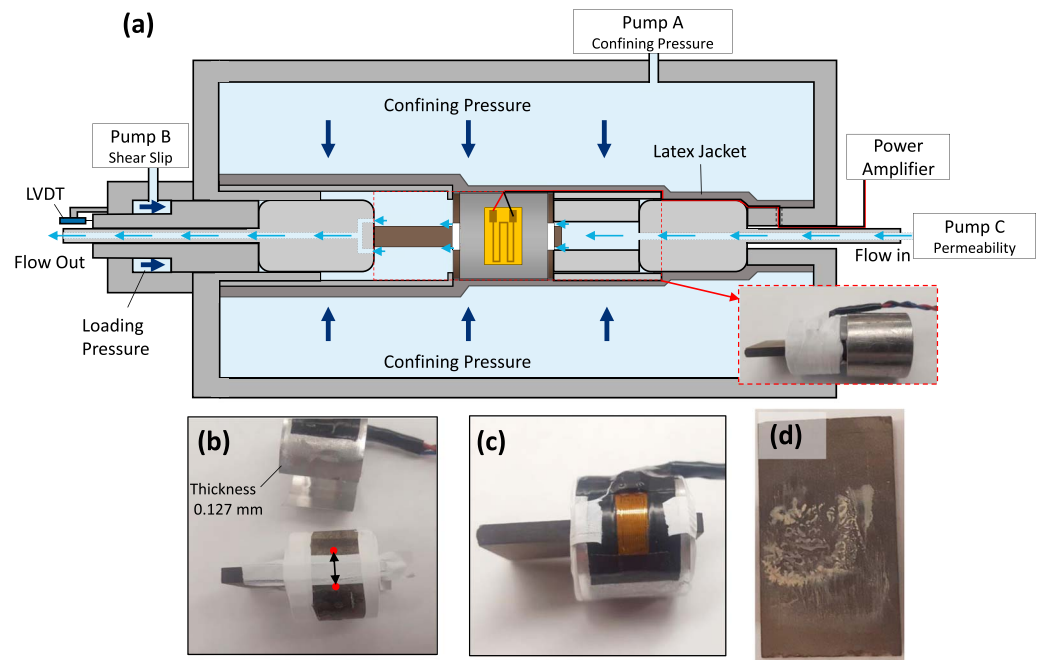
Figure 1. (a) Experimental configuration. (b) Green River shale sample before the strain gauge assembly (top) is added. The center block is continuous under the strain gage. Red dots represent fiducial locations for the measurement of cross-fracture displacement. (c) Sample with strain gauge assembled. This is further wrapped with PTFE tape before final installation (see Figure 1a bottom right inset). (d) Condition of fracture surface postexperiment. LVDT = linear variable differential transducer; PTFE = polytetrafluoroethylene.

We select apparently uniform surfaces of Green River shale, which is a clay-poor brittle shale (carbonate ~ 52%, tectosilicate ~ 46%, and phyllosilicate ~2%; Fang et al., 2017) deposited in a fresh water lacustrine environment (Grand Junction, Colorado). Green River shale is selected because it is hard enough to endure shear loading and the permeability decay during the hold is relatively fast and observable on laboratory timescales. The surfaces are initially flattened by wet abrasion to achieve suitable flatness and then ground with 60 grit aluminum oxide powder to create roughness.

Four experiments are conducted on three different samples. Two of the four experiments, KTS1 and KTS2, are consecutively conducted with the same sample. Surface wear products are washed off after KTS1, but no further surface grinding is conducted between the two experiments. Experiments are nominally designed to repeat 2-mm slips and 12-hr holds but are modified with consideration of flow rate, pressure, and remaining upstream reservoir volume (see Table 1 for detail). The pressure difference (ΔP) along the faults is designed to be maintained at 200 kPa, but due to the limited pump volume, it is adjusted from an initially low pressure to a later high pressure with maximum of 200 kPa. The loading rate for all slips is 10 μm/s.

2.2. Strain Gauge Measurement of Fracture Normal Deformation

Fracture normal deformation is measured by the strain gauge straddling the two fractures. The strain gauge is attached on a thin (0.127 mm) aluminum shim and placed on the side of the center block (Figures 1b and 1c). The gauge pattern fully covers the taped area with two anchoring points at the two ends (red dots marked in Figure 1b). The strain gauge measures relative displacement of the two half-cylindrical cores during the test—hence the dilation of the two-stacked fracture surfaces. To reduce this center block thickness effect, the strain gauge displacements are detrended. We note that, in the slip phase, there can be two artificial influences that are not related to fault opening: (i) lateral movement of the sample may directly influence the deformation of the aluminum shim and (ii) thickness change of the center block. However, the direct effect of sample lateral movement is principally concentrated in the initial slip phase (where friction between the sample and the polytetrafluoroethylene tape build up) and is not a major concern in our analysis.

Table 1
Experimental Procedures of Each Experiments

No.	Initial slip	Hold 1	Slip 1	Hold2	Slip 2	Hold 3	Slip 3	Hold 4	Slip 4	Remarks
KTN1	2.5 mm	8 hr	1.5 mm	12 hr	2 mm	12 hr	2 mm	12 hr	2 mm	
KTN2	5 mm	2 hr	1 mm	6 hr	2 mm	12 hr	2 mm	-	-	
KTS1	3 mm	8 hr	2 mm	12 hr	2 mm	12 hr	2 mm	-	-	Same sample
KTS2	3 mm	8 hr	2 mm	12 hr	2 mm	12 hr	2 mm	12 hr	2 mm	consecutive Profile measured (Figure 7)

A reference length must be identified to convert measured strain to fracture normal displacement. Two potential end-member reference lengths may be defined. When the deformation occurs entirely within the pattern length of the strain gauge (9.53 mm), then this pattern length can be used directly as a reference length. Conversely, if the deformation occurs over entire ring-shaped extent of the aluminum shim, the half circumference (~ 40 mm) should be used as the reference length (see Figure S1 for detail). The length of the shim contributing to the deformation can be estimated by force balance between the boundary force that drives the deformation of the shim (induced by compaction and dilation of the fracture) and the friction that resist that deformation. The force induced by fracture displacement δ over deformation length L is $F_s = E w_a h \delta / L$ where E is the deformation modulus of aluminum, h is the thickness of shim (0.127 mm), and w_a is the shim width. Conversely, the resisting frictional force is $F_f = \sigma \mu w_a L$ where σ is normal stress (3 MPa) and μ is friction coefficient. Equating F_s and F_f gives estimated deformation length L as

$$L = \sqrt{\frac{Eh\delta}{\sigma\mu}}. \tag{4}$$

Substituting $E = 69$ GPa (aluminum), $h = 0.127$ mm, and $\sigma = 3$MPa and assuming $\mu = 0.5$ yields a deformation length $L = 3.4$ mm for a fracture normal displacement $\delta = 2$ μm, implying that the few microns of repeated opening and compaction observed in these experiments (see Figure 4, following) likely occur within the strain gauge pattern area. Hence, in this work, we use the half of the pattern length as a reference length (*half* is used to measure single fracture normal displacement). However, we note that the large-scale compaction observed in the initial stage of the experiment may be underestimated since the deformation can extend beyond the strain gauge pattern length.

2.3. Surface Profile Measurement and Flow Simulation

Two consecutive experiments (KTS1 and KTS2) are conducted with the same set of samples and the same configuration (initial position and shear direction). Surface profiles are measured via optical profilometry before, in-between, and after these consecutive experiments to observe the evolution of surface asperities over the slip experiments. The measurements are conducted over a 5.5 × 5.5-mm patch of the surface with a spatial resolution of 1.6 μm. The measured surface patches are selected in the area where full slip is applied. The surfaces are air washed before the surface measurements are conducted.

To define the structure of permeability within the fault, we conduct flow simulations using the surface profile data. We assume that the opposite side of the fracture is flat, with this potentially leading to an underestimation of permeability. We do not consider other factors that reduce permeability, such as the presence of wear products and elastic compaction due to normal stress. To reduce the computational burden, 20 × 20 pixels (1 pixel–1.6 × 1.6 μm) are averaged and combined into a single node. Permeability at each node is calculated using the parallel plate approximation (cubic law, Reynolds equation). Since water is generally regarded as incompressible fluid, the two dimensional (*x-y* domain) steady state flow equation becomes

$$\frac{\partial}{\partial x}\left(\frac{b^3}{12\mu}\frac{\partial P}{\partial x}\right) + \frac{\partial}{\partial y}\left(\frac{b^3}{12\mu}\frac{\partial P}{\partial y}\right) = 0. \tag{5}$$

where b is aperture height. This equation is solved over the domain using the finite difference method.

Fluid flows horizontally across the fracture domain between opposite pressure boundaries transiting from 50 to 0 kPa on left and right sides of the fracture and with no flow boundaries at top and bottom. The pressure

difference (50 kPa over 5.5-mm flow) is scaled relative to the full fracture size (200 kPa for 25-mm flow). To analyze the permeability response to the compactions, the aperture is reduced by four different magnitudes: 0, 2, 3, and 4 μm. To avoid a singularity in the numerical solutions, a 1-nm aperture height is assigned on contacting surfaces.

3. Results

We explore cyclic permeability evolution during slide and then hold experiments on laboratory faults. The permeability evolution is converted into an equivalent hydraulic aperture and compared to the fault normal deformation directly measured by the straddling strain gauge. We then explore the evolution of surface topography observed in consecutive experiments. We use the measured surface topography to reconstruct fracture apertures and conduct flow simulations to analyze the characteristics of permeability structure in the fracture.

3.1. Permeability Evolution

Figure 2b presents the evolution of permeability for the entire (~ 45 hr) duration of the tests. The permeability evolution clearly demonstrates cyclic destruction of permeability during the hold periods and enhancement during reactivations. During most of the holds, permeability continuously declines without any evidence of stabilizing to a steady state. Conversely, during most of the reactivations, permeability significantly enhances. This cyclic destruction and enhancement of permeability becomes more evident with later sequences of holds-and-slips for three cases (KTN1, KTN2, and KTS2). For example, permeability response during the first slips at 8 hr does not show significant permeability enhancement for those three tests or even decreases for sample KTN1. However, the subsequent slips clearly and consistently enhance permeability.

Permeability response to initial slip is highlighted in Figure 2a, showing a strong destruction of permeability within a few millimeters of slip, in all cases (see Table 1 for initial slip distances). These strong destructive effects are consistent with previous observations (e.g., Fang et al., 2017; Im et al., 2018; Ishibashi et al., 2016) representing a strong shear-driven comminution of fracture asperities on artificially prepared surface. The comminution is apparently reflected by the generation of wear products as shown in Figure 1d. The generation of wear products further suggests that the permeability decreases are not only caused by effects of aperture decrease but also by clogging by the fine wear products that clog the aperture spaces.

Figure 2c shows friction response during the entire experiment. All deformation histories follow typical rate and state friction response (see inset in Figure 2c, Marone, 1998). The overall friction evolution appears to be similar to that of permeability (Figure 2c)—decays during holds and enhances during slips. However, friction responses are much more consistent without having the initial significant shear decay observed in permeability evolutions (Figure 2a).

Permeability continuously decreases during most of the holds. However, we observe one exception in experiment KTS1 in the initial 8-hr hold (dark red at 0–8 hr) as highlighted in Figure 2d. This shows permeability decline for the initial 5 hr but demonstrates occasional sudden fluctuations. These permeability fluctuations are initiated by adjustment of the pressure difference ΔP from 100 to 200 kPa at 5 hr. It is not surprising that the permeability is influenced by pore pressure perturbation (e.g., Candela et al., 2014, 2015). But the permeability continues to occasionally fluctuate for the next ~2 hr where the pressure is maintained at a constant 200 kPa (circle highlighted in Figure 2d). During these fluctuations, only slight dilation is recorded upon application of the pressure change but no clear signal is observed over any of the subsequent permeability fluctuations, implying that this is a nondilation related effect such as due to the intermittent transport of fine wear product and periodic clogging and unclogging. This reasoning is further supported by comparison with the result of KTS2. Experiments KTS1 and KTS2 are conducted sequentially with identical sample and experimental configurations. Therefore, the aperture height of KTS1 is unlikely to be smaller than KTS2. However, the permeability of KTS1 is significantly smaller than KTS2 during the initial hold (see Figure 2b initial 7 hr), implying that the dominant flow path is presumably clogged by wear products. Once the clogs appear to have been removed at 7 hr, permeability of KTS1 never decreases below that of KTS2.

Permeability responses during slips are shown as zoomed-in plots in Figures 2e–2g. During the slide phase, samples are sheared 2 mm at 10 μm/s with only a few exceptions (see Table 1). In all cases, permeability
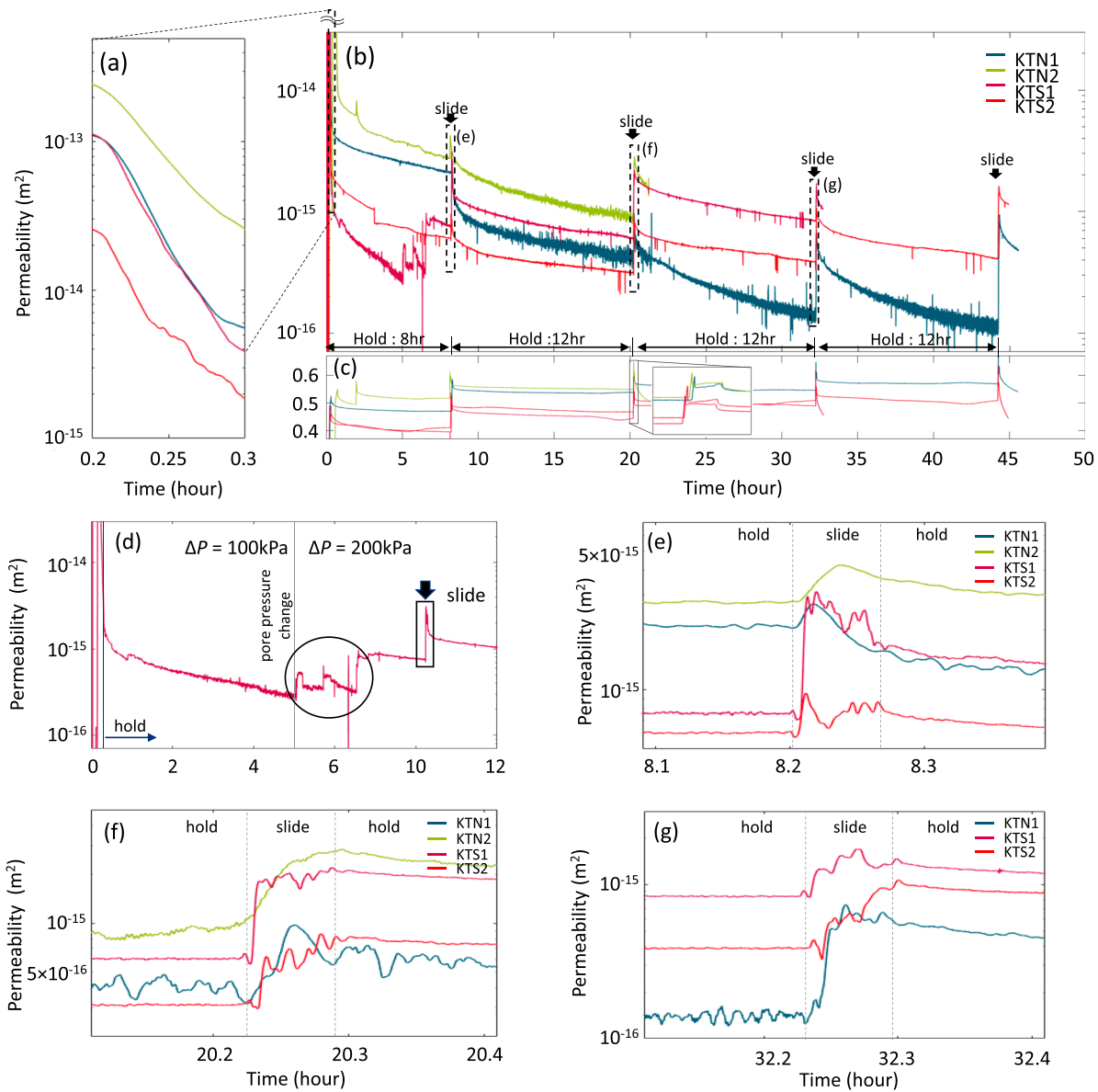
Figure 2. Permeability response to slide-hold-slide experiments (see Table 1 for detailed procedures for each experiment). (a) Permeability response to initial shearing-in. (b) Permeability response during the overall duration of the experiment (~45 hr). The pump in experiments KTN2 and KTS1 is depleted at ~21 and ~33hr, respectively. (c) Friction response during the overall experiment. (d) Step permeability changes observed during experimental hold of KTS1. (e–g) Zoomed-in view of shear permeability responses marked at Figure 2b.

increases at the beginning of the slip. However, the responses after this initial increase are varied and dissimilar. The first slips (Figure 2e) show that the permeability initially increases but soon begins to decrease as slip progresses. Conversely, permeability continues to increase with later stage slips (Figure 2g).

We use the cubic law to convert permeability into equivalent hydraulic apertures (equation (3)) and to allow comparison with observed shear dilation as in Figure 3. These results show a few microns of hydraulic aperture change corresponding to cyclic permeability decay during holds (vertical decline) followed by permeability enhancement upon slip. Overall, the permeability response appears to be continuous (dashed lines) with troughs associated with hold. This roughly continuous hydraulic aperture during slip may be defined (dashed line in Figure 3) as a *dynamic* aperture. The dynamic aperture significantly declines at initial stage of slips (corresponding to Figure 2a), representing shear comminution and potential wear product clogging, and then appears to stabilize as slip proceeds. During holds, as observed in Figure 3, the hydraulic aperture
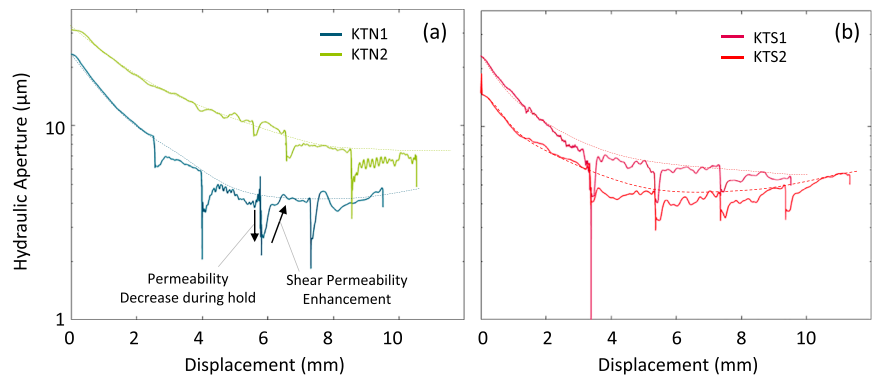
Figure 3. Evolution of hydraulic apertures calculated from the cubic law (equation (3)) using the permeability data of Figure 2b.

deviates from this dynamic aperture. However, when slip resumes, the hydraulic aperture recovers to the dynamic aperture and begins to repeat the same cycle.

3.2. Fault Normal Deformation

Figure 4a shows the evolution of normal displacement (Δb_s). Since zero displacement ($\Delta b_s = 0$) is set at zero confining stress, the initial stages of loading resulted in strong compactions (15–50 μm). KTS2 shows the smallest initial compactions as the experiment is conducted consecutively after KTS1, and therefore, its
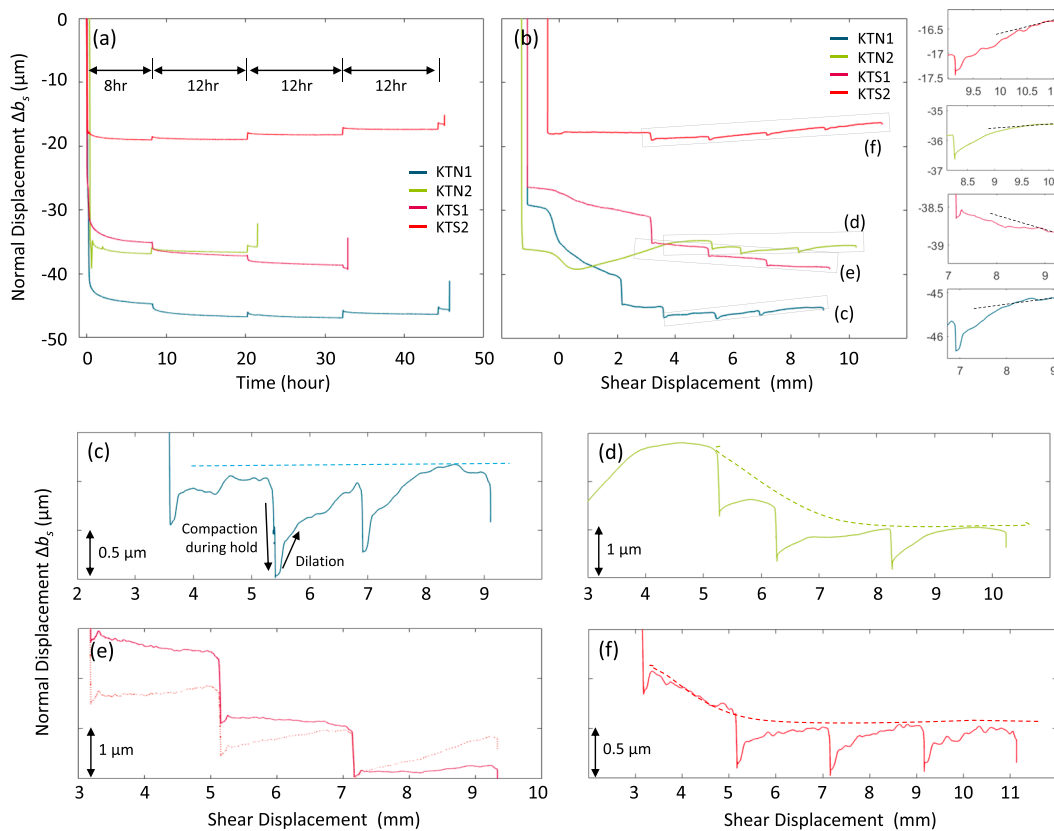

Figure 4. Fault normal deformations measured by circumferential strain gauge (Δb_s). (a and b) The fault normal deformation with time and then with shear displacement, respectively. (c–f) Zoomed-in view of normal displacement marked by rectangle in Figure 4b. The displacement in Figures 4c–4f is adjusted by the trend line shown on the right side of Figure 4b.

initial roughness is smaller than that of the other experiments. During holds, compactions are always observed without exception. The magnitudes of the compactive events are typically 0.5–1 µm.

Figure 4b presents fault normal deformation with slip, prior to detrending (identical results to Figure 4a). The initial strong compactions (vertical compactions) result from the application of confining stress. Over the following 2-mm slip, KTN1 and KTS1 show strong compaction that corresponds to permeability reductions (Figure 3). It is incongruous that the normal displacement of KTN 2 increases during the initial 2 mm of slip and seemingly inconsistent with the initial permeability reductions. However, the increase in the change in the normal displacement change here is likely an artifact that is induced by thickness change of a slightly tapered central rock block. Compaction rate significantly enhances after the conclusion of slips in all cases, indicating the asperity connection (real area of contact) is significantly loosened during the slips.

Since the strain gauge also measures the thickness change of center block, the fault normal deformation during slip should be detrended to estimate real aperture compaction/dilation. We use the later stage displacement as a reference trend (dashed lines on the right side of Figure 4b). Three of the detrended normal displacements (Figures 4c, 4d, and 4f) adequately represent the cyclic compaction during holds and shear-induced dilation. The shear dilation during those experiments is initially rapid and slow over the later stages as similarly observed in the trend for hydraulic aperture (Figure 3) recovered from the permeability measurements. The exception to this behavior (Figure 4e) still shows compaction during the hold, but dilation is not apparent with slip. Moreover, the evolution of normal displacement shown in Figure 4e is much flatter in time than the other cases showing that the permeability enhancement may not be solely dependent on aperture dilation. In fact, the magnitude of shear dilation observed in the other cases (Figures 4c, 4d, and 4f) is also typically smaller than the hydraulic aperture changes (Figure 3).

3.3. Static Compaction

Figure 5 illustrates compaction measured by the strain gauge (Δb_s, Figure 5a) and the evolution of hydraulic aperture change (Δb_h, Figure 5b) calculated from flow rate and the cubic law. Compaction evolves following a power law apparent from the near-linear plot in log-log space (Figures 5a and 5b). The power exponent (n) is uniformly of the order 0.2–0.4. Interestingly, this power law compaction rate is of similar range to that previously observed in solution-transport-driven indentation experiments (Gratier et al., 2014) and also observed for changes in hydraulic aperture on finely polished granite fractures (Im et al., 2018).

The magnitudes of the compactions in both cases are similar (0.5–4 µm) but not identical. Figure 5c compares the magnitudes of the two compactions at the end of holds, showing that they are positively correlated. However, generally, hydraulic aperture reductions (compactions, Δb_h) are larger than the strain gauge measurements (Δb_s) with two exceptions on the initial holds (circles in Figure 5c). The two fourth holds (stars) show a change in hydraulic aperture that is more than 2 times larger than the measured compaction ($2\Delta b_s < \Delta b_h$). This behavior can be influenced by the artificial effect of deformation of the aluminum (as noted in section 2), or it could also be a real physical response where compaction does not proceed and related to permeability reduction due to, for example, mineral precipitation (Yasuhara et al., 2003, 2004).

3.4. Surface Profile

Three consecutive surface scans are conducted on two consecutive experiments (KTS1 and KTS2; Figure 6). Figure 6a shows an initial surface profile scanned by white light optical profilometry over a window 5.5 × 5.5 mm in dimension and with spatial resolution of 1.6 µm. Vertical variations of the initial surface profile are mostly within ± 20 µm of the mean.

We observe strong comminution and flattening during the first experiment with a rough surface. Comparison between Figures 6a and 6b indicates that the peaks of the fresh initial surfaces (Figure 6a) are planed down after the experiment (Figure 6b). This significant comminution is apparent from the histogram of the surface scans. Figure 6d shows that initial asperity height that ranges up to ~ +20 µm (black) is reduced to ~ +10 µm after slips (red). The magnitude of the comminution is large in the first experiment (KTS1) but is significantly reduced for the second experiment (KTS2).

Figures 6e and 6f compare cross-sectional profiles of the initial rough surface (gray), after the first (KTS1, red) and second (KTS2, blue) experiments, aligned both along the slip direction (Figure 6e) and perpendicular to the slip direction (Figure 6f). Note that the red and blue curves represent identical surface locations on
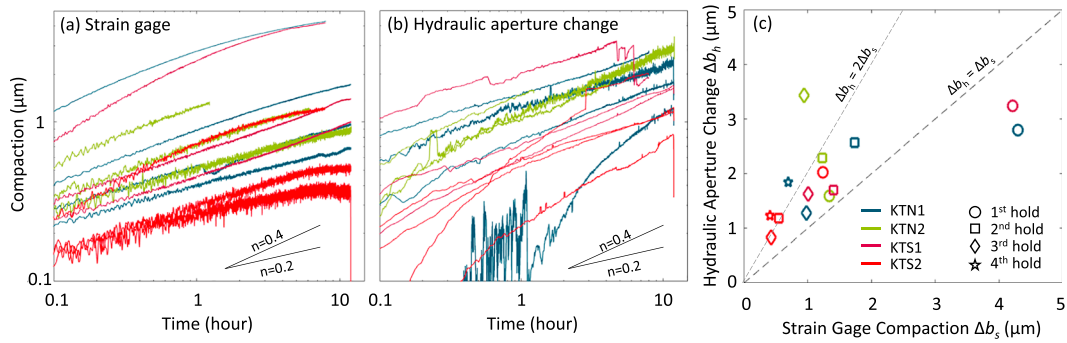
Figure 5. Compactions during holds observed via (a) direct measurement by strain gauge, Δb_s, and (b) equivalent hydraulic aperture calculated from the cubic law, Δb_h. (c) Comparison of the magnitude of final compactions between Δb_s and Δb_h. Axis ranges of Figures 5a and 5b are identical.

the sample. The observed roughness of the curves appear similar, but aperture height of the blue profile (before KTS2) is slightly smaller than that for the red profile (after KTS2) as similarly observed in the histogram in Figure 6d. Overall, the asperity height difference in Figures 6e and 6f appears to range from negligible magnitude (e.g., Figure 6f at ~ 3.5 mm) to a maximum of ~ 5 μm (Figure 6e at 0.5 mm) that roughly corresponds to the hydraulic aperture difference of KTS1 and KTS2 (~ 2 μm) shown in Figure 3b.
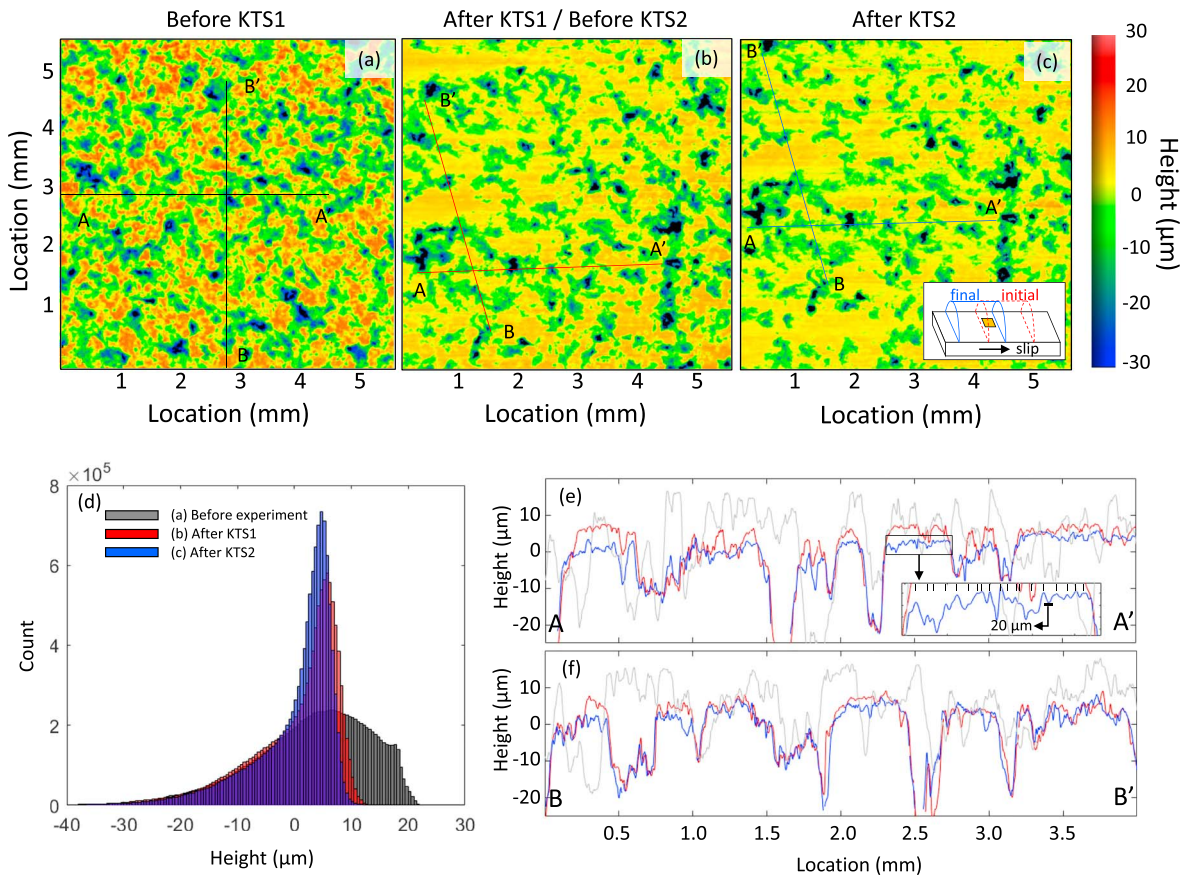

Figure 6. Surface profilometry measured consecutively over two consecutive experiments, KTS1 and KTS2: (a) initial laboratory surface (before KTS1), (b) surface profile after the first experiment, and (c) surface profile after the second experiment. Note that Figures 6b and 6c are roughly identical locations on the surface while Figure 6a is at different locations. (d) Histograms of surface heights. The *x* axes of the initial surfaces are adjusted to exhibit similar tails (negative heights) to compare the effects of comminution directly. (e and f) Cross section of surface profile. Location and color correspond to the lines shown in Figures 6a–6c. Red and blue profiles show identical locations in the sample both before and after the second experiment while gray is at a different location.
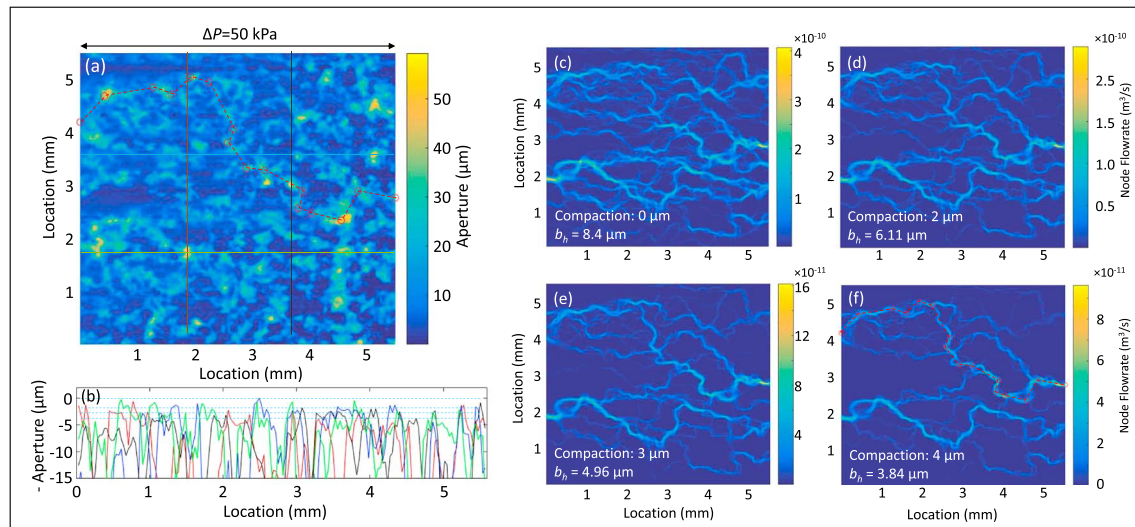
Figure 7. (a) Aperture heights of a noncompacted surface constructed from the surface profile of Figure 6b. (b) Cross sections of aperture heights with color corresponding to the line in Figure 7a. Dashed horizontal lines show the level of compaction applied for the simulation results. (c–f) Simulation results. Applied compactions and resulting equivalent hydraulic aperture are presented to the bottom left of each result. Red dashed lines in Figures 7a and 7f indicate the same locations showing major flow channel developing by the connecting of the major previously disconnected surface troughs.

Major troughs on these surfaces (i.e., high permeability zones) are developed during initial surface grinding using rough (60 grit) abrasives. However, we also observe a smaller-scale roughness developed on the top of the planed surface. Inset of Figure 6e highlights this smaller-scale roughness and shows that the spacing of the local peaks (vertical line) is of the order of ~10–20 μm. Apparently, major flow channels develop by connecting the initially disjoint major troughs and flow conduits. Once the major troughs are well connected, permeability of this system is dominated by this connected network. Conversely, if these troughs do not become well connected (for example, by shear flattening and chemo-mechanical compaction) fluid must be transported only through the small-scale roughness that acts as bottlenecks to the major flow channels. In this case, the overall permeability is controlled by the permeability of the bottleneck. To address this complex permeability structure, we conduct flow simulations using the surface profiles.

3.5. Flow Simulation

Surface profiles in Figure 6 imply two major contributions to surface roughness: (i) surface grinding before experiments that generates deep, larger-scale major troughs and grooves and (ii) experimental slips that generate a smaller-scale roughness developed on the real contact area. Apparently, the larger-scale roughness controls development of major flow paths—impacting permeability structure. Conversely, the small-scale roughness developed by the experimental slips should control the friction and chemo-mechanical compaction, since it is developed over the real area of contact. If the deep troughs that are developed on the surface are well connected, the compactive processes resulting from the small-scale roughness may not be capable of inducing the significant permeability evolution observed in this experiment. To explain how permeability evolution is controlled by small-scale compaction and to define the permeability structures in the fault zone, we conducted steady state fluid flow simulations.

Numerical simulation results of steady state fluid flow (Figures 7c–7f) illustrate the development of channels with increased fracture compaction. Initially, diverse channels are developed on the noncompacted surface (Figure 7c) but as compaction proceeds, a few major channels dominate in carrying the overall flow rate (Figure 7f). The channels develop by connecting major troughs created during the initial surface grinding. The red dashed line in Figure 7a represents one of the major flow channels developed after 4-μm compaction (red dashed line in Figure 7f). Apparently, the flow channel develops by connecting major troughs, showing that the distribution of troughs is important in defining permeability of the fault.

To estimate the hydraulic aperture of system, total flow rate to the outflow boundary is converted into an hydraulic aperture (b_h) using a cubic law and presented in Figures 7c–7f (bottom left). The magnitude of
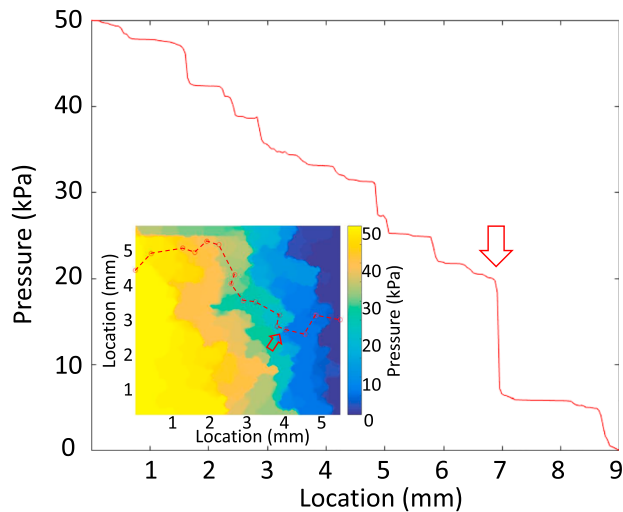
Figure 8. Pressure together with major flow channels at 4-μm compaction (red dashed line in inset and Figures 7a and 7f). Inset: pressure distribution of the simulation result. Red arrow corresponds to the location of the red arrow in the inset.

flow rate (hydraulic aperture 3.84–8.4 μm) corresponds to the hydraulic apertures observed in our experiments (Figure 3). Reduction of the hydraulic aperture is slightly larger than the applied compaction. For example, a total compaction of 4 μm yields 4.56 μm of hydraulic compaction (from 8.4 to 3.84 μm; Figures 7–7f). This may result from the spatial closing of fluid channels and partly explains the observation that hydraulic compaction is generally larger than normal displacement (Figure 5).

Figure 8 shows the pressure distribution along the major flow channel (red dashed line in Figures 7a and 7f and 8 inset) at 4-μm compaction (Figure 7f). The pressure distribution illustrates occasional step-like pressure drops, implying that the flow rate is controlled by several low permeability zone bottlenecks. For example, ~30% of the total pressure drop occurs at only one bottleneck (red arrows). This result shows that the permeability of the overall fracture system is effectively controlled by the aperture at the bottleneck developed over a major flow path.

4. Discussion

Our experiments replicate cycles of slow permeability reduction and earthquake-induced permeability enhancement observed in nature (Elkhoury et al., 2006; Xue et al., 2013). Permeability decline and enhancement are associated with fault compaction and dilation. However, the measured compaction and hydraulic aperture change are not completely coupled. Here we discuss possible mechanisms of the permeability changes.

4.1. Permeability Decay, Compaction, and Matedness

We show that the sealing is accompanied by aperture compaction during static loading indicative of mineral dissolution processes contributing to sealing during hold periods. Compactions both directly measured by strain gauge and inferred/calculated from flow rates track together and follow power law decay with a power exponent of ~0.2–0.4. The slow and continuous process of compaction implies that it is likely a result of chemo-mechanical process such as pressure solution, stress corrosion, and mineral precipitation (Dove & Crerar, 1990; Lehner, 1995; Yasuhara et al., 2003, 2004; Yasuhara & Elsworth, 2008). Such power law compaction is consistent with similarly observed solution-driven intrusion of a stressed rigid indenter (Gratier et al., 2014).

Measured compaction (Δb_s) and hydraulic aperture change (Δb_h) are similar in magnitude at ~0.5–4 μm during ~8–12 hr of hold. The two compactions show strong positive correlations, but their magnitudes are not identical. Generally, the hydraulic aperture change Δb_h appears to be larger than the mechanical compaction Δb_s except for the first two hold cases (Figure 5). We note that this behavior ($\Delta b_h > \Delta b_s$) can be an artifact due to deformation of the aluminum sheath extending beyond the extent of the strain gauge pattern. Separate from this artifact, there are several plausible mechanisms that can explain such behavior. Spatial closing of flow path is one possibility as observed in the results of flow simulation (Figure 7). Also, mineral precipitation is another candidate as it can significantly reduce permeability without the need for mechanical compaction (Yasuhara et al., 2003, 2004). The opposite behavior ($\Delta b_h < \Delta b_s$) is only observed during the first holds, where the flow rate is relatively larger than the other cases and therefore the influence of mineral precipitation is likely smaller and particle mobility of fine wear products is higher.

Since the compaction may be driven by mineral dissolution over the microscopic contact, which is not necessarily aligned with the mesoscale fracture orientation, it may lead to an increase in the matedness of the fault. Figure 9 illustrates hypothetical compaction processes using two 1-mm lengths of the surface profiles shown in Figure 6b. The two profiles of the upper and lower surfaces are taken from the planed-down surface along slip direction (blue lines in Figure 9a). The surface profiles (e.g., Figure 9b) show that microscale roughness exists even on these planed-down surfaces. This small-scale roughness is also observed and shown to be independent of the slip directions (Candela & Brodsky, 2016). Assuming that mineral dissolution rates are identical between the upper and lower surfaces, Figure 9 shows that significant mating can result from
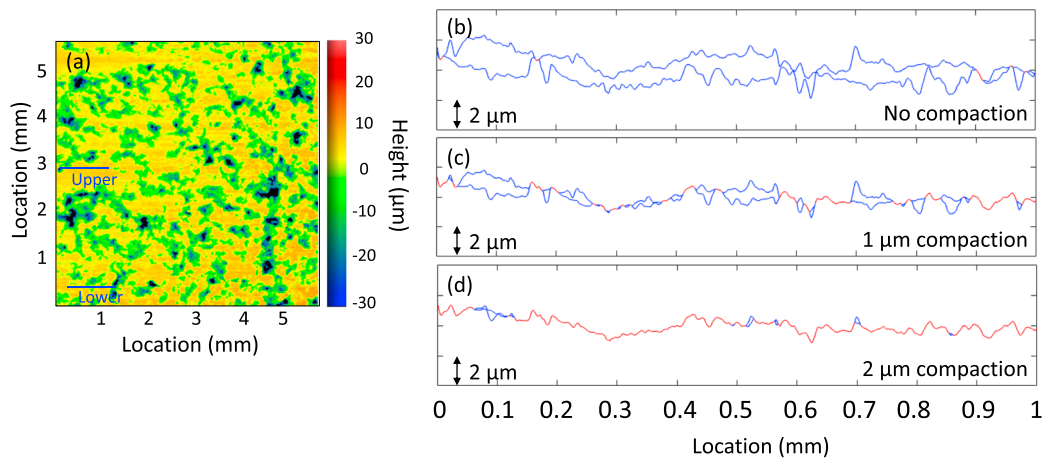
Figure 9. Hypothetical compaction of fine-scale roughness developed on the sheared surface. (a) Surface profile (identical to Figure 6b). (b–d) Hypothetical compaction driven by mineral dissolution at the real contact (red). The surface is taken from the flattened surface shown in Figure 9a. Identical dissolution rate on upper and lower surfaces is assumed.

the magnitude of compaction we observe in our experiments (~1–2 μm). As dissolution proceeds (Figures 9b ➔ 9c ➔ 9d), real area of contact (red) increases. Since the microscopic real contact is not parallel to the mesoscale contact surface as shown in Figure 9, the compaction process increases matedness. Figure 9d illustrates this strongly mated hypothetical contact.

4.2. Mechanism of Permeability Enhancement

Permeability response to slip is controlled by preslip sealing (Im et al., 2018). If slip is applied on the unsealed surface (e.g., Figure 9b), significant comminution and consequent permeability destruction will occur. This explains the initial shear-driven strong permeability reduction on fresh surfaces (Figure 2a). Conversely, if slip is applied on the surface that has been strongly sealed as shown in Figure 9d, the established seal may be breached by slip and accordingly induce permeability enhancement. Figure 3 shows that the hydraulic aperture (permeability) is approximately maintained at the level of ~5–10 μm during the slip defining a dynamic hydraulic aperture. If we assume that there is a constant dynamic hydraulic aperture, the magnitude of shear permeability enhancement should directly scale to the magnitude of preslip compaction. This simple assumption explains previous observations of larger permeability enhancement associated with larger preslip sealing (Im et al., 2018).

Most of the shear permeability enhancements are associated with dilation in these experiments. However, we also observe some behaviors that are different from this norm where the permeability enhancements are not well coupled with aperture changes in experiment KTS1 (Figure 4e). This experiment (KTS1) demonstrates sudden permeability fluctuations presumably driven by particle mobilization (Figure 2d). Interestingly, permeability enhancement with slip in KTS1 similarly appears as a step increase at the initiation of shear deformation (Figure 10a; also Figures 2 and 3), implying that such particle mobilization may also be triggered by the initiation of slip. Throughout all experiments, we observe two significantly different permeability enhancement behaviors with slip: (i) sudden permeability enhancement that is dominant at the initiation of slip (Figure 10a) and (ii) gradual and continuous permeability enhancement with slip (Figure 10b). The sudden permeability enhancements are often shown in earlier stage slips. Conversely, gradual displacement-dependent permeability enhancement is more general in later slips (comparing Figures 2d and 2f). The result implies that particle mobilization and unclogging may also be triggered by slip and contribute to the shear permeability enhancement process. However, the detailed mechanism of shear-driven unclogging remains unclear.

4.3. Implications for Natural Systems

Our experiments on laboratory faults substantially replicate permeability cycles observed in nature—albeit at different timescales. We observe that shear permeability enhancement requires preslip sealing. Indeed, gradual permeability decay of the natural hydraulic system during the interseismic period is a well-
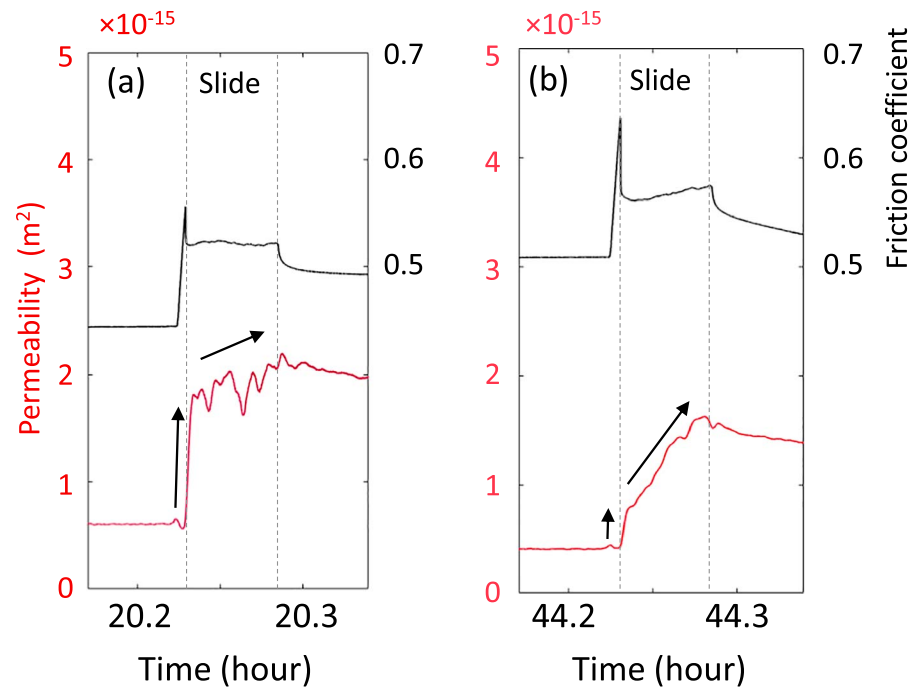
Figure 10. Two different permeability evolution behaviors (red) with friction (black). (a) Significant initial permeability increase at initiation of slip followed by moderate gradual increase (KTS1 second slip). (b) Small initial permeability increase at initiation of slip followed by significant permeability enhancement (KTS2 fourth slip).

documented phenomenon (Elkhoury et al., 2006; Wang et al., 2016; Xue et al., 2013). The slow and gradual nature of the permeability decay during interseismic periods implies that the sealing may be driven by chemo-mechanical processes such as pressure solution and stress corrosion (Yasuhara et al., 2003, 2004; Yasuhara & Elsworth, 2008). Since mineral dissolution rate is significantly dependent on temperature and applied stress (Dove & Crerar, 1990), compaction of natural faults during the interseismic period should be more significant than in our experiments due to higher temperatures, larger normal stresses, and longer duration in nature. Accordingly, the contacting surfaces are likely strongly mated in their natural state. Indeed, highly mated natural faults are reported from profiling of opposing surfaces (Power & Tullis, 1992).

Slip on the strongly mated contact will breach the interlocking of the surfaces and induce dilation. Therefore, the coseismic permeability enhancement observed in nature can be significantly contributed to shear breaching and dilation of the sealed/mated surface. Further, this result suggests that the observation of permeability enhancement induced by distant earthquakes (Brodsky et al., 2003; Manga et al., 2012) may directly result from remotely triggered seismicity. So far, this behavior has been explained by flux-driven unclogging of colloidal seals (Brodsky et al., 2003; Candela et al., 2014, 2015; Elkhoury et al., 2011), which is also presumed in our experiment. Our experiments suggest that remotely triggered fault shear (e.g., Hill et al., 1993; Van der Elst et al., 2013) should also be considered as a mechanism for this permeability enhancement.

5. Conclusion

We observe cycles of permeability enhancement and reduction during slide-hold-slide experiments constrained by concurrent measurements of fault normal deformation via a strain gauge. The experimental results demonstrate that permeability response to slip is controlled by preslip sealing. During hold periods, fault normal deformation and hydraulic aperture compaction follow power law decay with a power exponent of ~ 0.2–0.4. The magnitude of the two (hydraulic and mechanically measured) compactions shows a strong positive correlation but is not identical. Generally, hydraulic aperture decline is larger than the measured compaction with two exceptions at first holds. Shear permeability enhancements are also

accompanied by shear dilation but again with some exceptions. Those observations imply that permeability cycles observed during fault repose and reactivation are controlled by chemo-mechanical compaction and mated surface dilation. However, there are more factors that can contribute to the complex behavior, such as mobilization of wear products.

Surface profile scans postexperiment show significant comminution during the experiments. This observation explains the strong permeability reduction observed during the initial shear-in of fresh laboratory prepared surfaces. The comminution effect is significantly reduced when the sample is reused for a consecutive test. Microscale roughness is developed on the top of the planed surface. We note that the magnitude of compaction observed in the experiment (a few microns) may increase the matedness of those microroughness contacts. If the mated contacts behave as a bottleneck on major flow paths, they can control overall permeability. Breaching the mated seal via slip can significantly enhance permeability.

References

Brodsky, E. E., Gilchrist, J. J., Sagy, A., & Collettini, C. (2011). Faults smooth gradually as a function of slip. *Earth and Planetary Science Letters*, *302*(1–2), 185–193. https://doi.org/10.1016/j.epsl.2010.12.010

Brodsky, E. E., Roeloffs, E., Woodcock, D., Gall, I., & Manga, M. (2003). A mechanism for sustained groundwater pressure changes induced by distant earthquakes. *Journal of Geophysical Research*, *108*(B8), 2390. https://doi.org/10.1029/2002JB002321

Candela, T., & Brodsky, E. E. (2016). The minimum scale of grooving on faults. *Geology*, *44*(8), 603–606. https://doi.org/10.1130/G37934.1

Candela, T., Brodsky, E. E., Marone, C., & Elsworth, D. (2014). Laboratory evidence for particle mobilization as a mechanism for permeability enhancement via dynamic stressing. *Earth and Planetary Science Letters*, *392*, 279–291. https://doi.org/10.1016/j.epsl.2014.02.025

Candela, T., Brodsky, E. E., Marone, C., & Elsworth, D. (2015). Flow rate dictates permeability enhancement during fluid pressure oscillations in laboratory experiments. *Journal of Geophysical Research: Solid Earth*, *120*, 2037–2055. https://doi.org/10.1002/2014JB011511

Candela, T., Renard, F., Bouchon, M., Schmittbuhl, J., & Brodsky, E. E. (2011). Stress drop during earthquakes: Effect of fault roughness scaling. *Bulletin of the Seismological Society of America*, *101*(5), 2369–2387. https://doi.org/10.1785/0120100298

Chen, J., Verberne, B. A., & Spiers, C. J. (2015). Interseismic re-strengthening and stabilization of carbonate faults by "non-Dieterich" healing under hydrothermal conditions. *Earth and Planetary Science Letters*, *423*, 1–12. https://doi.org/10.1016/j.epsl.2015.03.044

Davidesko, G., Sagy, A., & Hatzor, Y. H. (2014). Evolution of slip surface roughness through shear. *Geophysical Research Letters*, *41*, 1492–1498. https://doi.org/10.1002/2013GL058913

Dove, P. M., & Crerar, D. A. (1990). Kinetics of quartz dissolution in electrolyte solutions using a hydrothermal mixed flow reactor. *Geochimica et Cosmochimica Acta*, *54*(4), 955–969. https://doi.org/10.1016/0016-7037(90)90431-J

Elkhoury, J. E., Brodsky, E. E., & Agnew, D. C. (2006). Seismic waves increase permeability. *Nature*, *441*, 1135–1138. https://doi.org/10.1038/nature04798

Elkhoury, J. E., Niemeijer, A., Brodsky, E. E., & Marone, C. (2011). Laboratory observations of permeability enhancement by fluid pressure oscillation of in situ fractured rock. *Journal of Geophysical Research*, *116*, B02311. https://doi.org/10.1029/2010JB007759

Elsworth, D., & Goodman, R. (1986). Characterization of rock fissure hydraulic conductivity using idealized wall roughness profiles.pdf. *International Journal of Rock Mechanics and Mining Sciences*, *23*(3), 233–243.

Fang, Y., Elsworth, D., Ishibashi, T., & Zhang, F. (2018). Permeability evolution and frictional stability of fabricated fractures with specified roughness. *Journal of Geophysical Research: SolidEarth*, *123*, 9355–9375. https://doi.org/10.1029/2018JB016215

Fang, Y., Elsworth, D., Wang, C., Ishibashi, T., & Fitts, J. P. (2017). Frictional stability-permeability relationships for fractures in shales. *Journal of Geophysical Research: Solid Earth*, *122*, 1760–1776. https://doi.org/10.1002/2016JB013435

Faoro, I., Niemeijer, A., Marone, C., & Elsworth, D. (2009). Influence of shear and deviatoric stress on the evolution of permeability in fractured rock. *Journal of Geophysical Research*, *114*, B01201. https://doi.org/10.1029/2007JB005372

Giger, S. B., Tenthorey, E., Cox, S. F., & Gerald, J. D. F. (2007). Permeability evolution in quartz fault gouges under hydrothermal conditions. *Journal of Geophysical Research*, *112*, B07202. https://doi.org/10.1029/2006JB004828

Gratier, J. P., Renard, F., & Vial, B. (2014). Postseismic pressure solution creep: Evidence and time-dependent change from dynamic indenting experiments. *Journal of Geophysical Research: Solid Earth*, *119*, 2764–2779. https://doi.org/10.1002/2013JB010768

Guglielmi, Y., Cappa, F., Avouac, J., Henry, P., & Elsworth, D. (2015). Seismicity triggered by fluid injection-induced aseismic slip. *Science*, *348*(6240), 1224–1226. https://doi.org/10.1126/science.aab0476

Hill, D. P., Reasenberg, P. A., Michael, A., Arabaz, W. J., Beroza, G., Brumbaugh, D., et al. (1993). Seismicity remotely triggered by the magnitude 7.3 Landers, California, earthquake. *Science*, *260*(5114), 1617–1623. https://doi.org/10.1126/science.260.5114.1617

Im, K., Elsworth, D., & Fang, Y. (2018). The influence of preslip sealing on the permeability evolution of fractures and faults. *Geophysical Research Letters*, *45*, 166–175. https://doi.org/10.1002/2017GL076216

Ishibashi, T., Asanuma, H., Fang, Y., Wang, C., & Elsworth, D. (2016). Exploring the link between permeability and strength evolution during fracture shearing: Proceedings: 50th US Rock Mechanics/Geomechanics Symposium Houston, Texas.

Junger, J. A., & Tullis, T. E. (2003). Fault roughness and matedness suggest significant fault-interface dilatancy with slip. EOS Trans. Am. Geophys. Union: Abstr. S51B-03.

Lehner, F. (1995). A model for intergranular pressure solution in open systems. *Tectonophysics*, *245*, 153–170.

Manga, M., Beresnev, I., Brodsky, E. E., Elkhoury, J. E., Elsworth, D., Ingebritsen, S. E., et al. (2012). Changes in permeability caused by transient stresses: Field observations, experiments and mechanisms. *Reviews of Geophysics*, *50*, RG2004. https://doi.org/10.1029/2011RG000382

Manga, M., Brodsky, E. E., & Boone, M. (2003). Response of streamflow to multiple earthquakes. *Geophysical Research Letters*, *30*(5), 1214. https://doi.org/10.1029/2002GL016618

Marone, C. (1998). Laboratory-derived friction laws and their application to seismic faulting. *Annual Review of Earth and Planetary Sciences*, *26*(1), 643–696. https://doi.org/10.1146/annurev.earth.26.1.643

Mukuhira, Y., Moriya, H., Ito, T., Asanuma, H., & Haring, M. (2017). Pore pressure migration during hydraulic stimulation due to permeability enhancement by low-pressure subcritical fracture slip. *Geophysical Research Letters*, *44*, 3109–3118. https://doi.org/10.1002/2017GL072809

Niemeijer, A., Marone, C., & Elsworth, D. (2008). Healing of simulated fault gouges aided by pressure solution: Results from rock analogue experiments. *Journal of Geophysical Research*, *113*, B04204. https://doi.org/10.1029/2007JB005376

Olsen, M. P., Scholz, C. H., & Léger, A. (1998). Healing and sealing of a simulated fault gouge under hydrothermal conditions: Implications for fault healing. *Journal of Geophysical Research*, *103*(B4), 7421–7430. https://doi.org/10.1029/97JB03402

Polak, A., Elsworth, D., Yasuhara, H., Grader, A. S., & Halleck, P. M. (2003). Permeability reduction of a natural fracture under net dissolution by hydrothermal fluids. *Geophysical Research Letters*, *30*(20), 2020. https://doi.org/10.1029/2003GL017575

Power, W. L., & Tullis, T. E. (1992). The contact between opposing fault surfaces at Dixie Valley, Nevada, and implications for fault mechanics. *Journal of Geophysical Research*, *97*(B11), 15,425–15,435. https://doi.org/10.1029/92JB01059

Power, W. L., Tullis, T. E., Brown, S. R., Boitnott, G. N., & Scholz, C. H. (1987). Roughness of natural fault surfaces. *Geophysical Research Letters*, *14*(1), 29–32.

Renard, F., & Candela, T. (2017). Scaling of fault roughness and implications for earthquake mechanics. In M. Y. Thomas, T. M. Mitchell, & H. S. Bhat (Eds.), *Fault zone dynamic processes: Evolution of fault properties during seismic rupture* (Chap. 10, Vol. 227, pp. 197–216). Hoboken, NJ: John Wiley. https://doi.org/10.1002/9781119156895.ch10

Tesei, T., Carpenter, B. M., Giorgetti, C., Scuderi, M. M., Sagy, A., Scarlato, P., & Collettini, C. (2017). Friction and scale-dependent deformation processes of large experimental carbonate faults. *Journal of Structural Geology*, *100*, 12–23. https://doi.org/10.1016/j.jsg.2017.05.008

Van der Elst, N., Savage, H., Keranen, K., & Abers, G. (2013). Enhanced remote earthquake triggering at fluid-injection sites in the Midwestern United States. *Science*, *341*.

Wang, C., Elsworth, D., & Fang, Y. (2017). Influence of weakening minerals on ensemble strength and slip stability of faults. *Journal of Geophysical Research: Solid Earth*, *122*, 7090–7110. https://doi.org/10.1002/2016JB013687

Wang, C., & Manga, M. (2015). New streams and springs after the (2014) M_w6.0 South Napa earthquake. *Nature Communications*, *6*, 1–6. https://doi.org/10.1038/ncomms8597.

Wang, C.-Y., Liao, X., Wang, L.-P., Wang, C.-H., & Manga, M. (2016). Large earthquakes create vertical permeability by breaching aquitards. *Water Resources Research*, *52*, 5923–5937. https://doi.org/10.1002/2016WR018893

Witherspoon, P. A., Wang, J. S. Y., Iwai, K., & Gale, J. E. (1980). Validity of cubic law for fluid flow in a deformable rock fracture. *Water Resources Research*, *16*(6), 1016–1024. https://doi.org/10.1029/WR016i006p01016

Xue, L., Li, H.-B., Brodsky, E. E., Xu, Z.-Q., Kano, Y., Wang, H., et al. (2013). Continuous permeability measurements record healing inside the Wenchuan earthquake fault zone. *Science*, *340*, 1555–1559. https://doi.org/10.1126/science.1237237

Yasuhara, H., & Elsworth, D. (2008). Compaction of a rock fracture moderated by competing roles of stress corrosion and pressure solution. *Pure and Applied Geophysics*, *165*(7), 1289–1306. https://doi.org/10.1007/s00024-008-0356-2

Yasuhara, H., Elsworth, D., & Polak, A. (2003). A mechanistic model for compaction of granular aggregates moderated by pressure solution. *Journal of Geophysical Research*, *108*(B11), 2530. https://doi.org/10.1029/2003JB002536

Yasuhara, H., Elsworth, D., & Polak, A. (2004). Evolution of permeability in a natural fracture: Significant role of pressure solution. *Journal of Geophysical Research*, *109*, B03204. https://doi.org/10.1029/2003JB002663

Yasuhara, H., Polak, A., Mitani, Y., Grader, A. S., Halleck, P. M., & Elsworth, D. (2006). Evolution of fracture permeability through fluid-rock reaction under hydrothermal conditions. *Earth and Planetary Science Letters*, *244*(1–2), 186–200. https://doi.org/10.1016/j.epsl.2006.01.046

Zhang, S., Tullis, T. E., & Scruggs, V. J. (1999). Permeability anisotropy and pressure dependency of permeability in experimentally sheared gouge materials. *Journal of Structural Geology*, *21*(7), 795–806. https://doi.org/10.1016/S0191-8141(99)00080-2

Zoback, M. D., Kohli, A., Das, I., & McClure, M. (2012). The importance of slow slip on faults during hydraulic fracturing stimulation of shale gas reservoirs. *SPE Journal*, SPE 155476. https://doi.org/10.2118/155476-MS